Journal Name

RSCPublishing

ARTICLE

Synthesis, Characterisation and Properties of Rare Earth Oxyselenides $A_4O_4Se_3$ (A = Eu, Gd, Tb, Dy, Ho, Er, Yb and Y)

Cite this: DOI: 10.1039/x0xx00000x

Received ooth January 2012,
Accepted ooth January 2012

DOI: 10.1039/x0xx00000x

www.rsc.org/

Andrew J. Tuxworth,[a] Chun-Hai Wang,[a] and John S.O. Evans [a,]*

Abstract: Rare earth oxyselenides $A_4O_4Se_3$ (A = Nd, Sm, Eu, Gd, Tb, Dy, Ho, Er, Yb and Y) were synthesised using solid state reactions and three new structure types (β, γ, and δ) were observed. $A_4O_4Se_3$ materials adopt either the α (A = Nd, Sm), β (A = Eu), γ (A = Gd, Tb) or δ (A = Dy, Ho, Er, Yb, Y) structure depending on the rare earth radius. Each structure type contains alternating $[A_2O_2]^{4+}$ and Se^{2-}/Se_2^{2-} layers. Different ordered and disordered arrangements of Se^{2-} and $[Se\text{-}Se]^{2-}$ gives the Se layer flexibility and leads to the four different structure types observed. The volume coefficients of expansion for $A_4O_4Se_3$ ranged from $+1.746(9) \times 10^{-5}$ to $+2.237(3) \times 10^{-5}$ K^{-1} from 12 to 300 K; no structural phase transitions were observed in this temperature range. Diffuse reflection spectra shows $A_4O_4Se_3$ are semiconductors with band gap E_g 1.02-1.46 eV. $Gd_4O_4Se_3$, $Dy_4O_4Se_3$, and $Tb_4O_4Se_3$ samples show antiferromagnetic ordering with Néel temperature, T_N, of 7 – 9 K. DFT calculations confirm the two different valence states of Se^{2-} and Se_2^{2-} in $Eu_4O_4Se_3$.

Introduction

Rare earth oxychalcogenides containing both oxygen and a second group 16 element (S, Se, Te) anion have a number of potentially important properties and applications. For example there have been many studies on doped Ln_2O_2S systems as optical and X-ray phosphors and ceramic scintillators. Gd_2O_2S:Tb is used in X-ray imaging; [1-3] $Y_2O_2S:Eu^{3+}$ is a well-known red phosphor.[1, 4] The high visible light extinction of $A_4O_4Se_3$ (A = Nd, Sm, Gd to Ho) nanoplates has also recently been reported as giving potential application in light filters and solar cells.[5] In this paper we report the first bulk synthesis of $A_4O_4Se_3$ materials for the smaller rare-earth elements Eu-Ho, i.e. those with ionic radii[6] $R_{VIII}(A^{3+}) < 1.066$ Å and describe their magnetic and physical properties.

Ternary rare-earth oxyselenides are known with a variety of A:O:Se ratios. Four compositions have been reported from conventional solid state routes: $A_{10}OSe_{14}$ (A = La-Nd),[7-9] A_2OSe_2 (A = Pr & Gd),[7, 10] $A_4O_4Se_3$ (A = La-Nd, Sm)[7, 11, 12] and A_2O_2Se (A = La, Pr, Nd, Sm, Gd, Er, Ho, Yb).[7, 13] A liquid phase synthesis of nanoplates of $A_4O_4Se_3$ (A = Nd, Sm, Gd-Ho) has also been reported.[5]

The oxygen-rich rare earth oxychalcogenides such as those investigated here have structures in which the hard/soft anions segregate into layers. For the majority of A_2O_2Q (Q = S, Se) phases the structure is made up of layers of A_4O tetrahedra which share 3 edges in trigonal space group $P\bar{3}m1$. Q^{2-} ions lie between these layers with each Q in an octahedral coordination environment. Each A site is thus 7 coordinate with four short bonds to O and three longer bonds to S (4O + 3S), Figure 1. For A_2O_2Te (A = La–Nd, Sm–Ho)[14-16] the A_4O tetrahedra share four edges leading to fluorite-like 2D slabs and a tetragonal unit cell with a ≈ 4 Å. The layers are analogous to those found in, for example, Aurivillius phases and the LaOFeAs superconductors. The Q^{2-} ion is then in 8 fold square prismatic coordination and the A^{3+} site is in a (4O + 4Se) distorted square antiprism. The change from sharing 3 to 4 tetrahedral edges increases the area per 2+ charge of the $[M_2O_2]^{2+}$ layers by ~13.4% to accommodate the larger Te^{2-}. Bi_2O_2S and Bi_2O_2Se have closely related structures.[17, 18]

$A_4O_4Se_3$ (or $A_2O_2Se_{1.5}$) materials have been prepared as bulk phases and structurally characterised for A = La, Ce, Pr, Nd and Sm and have the same layered structures.[12] These systems contain a mixture of Se^{2-} and Se_2^{2-} anions, and the consequent increased number of Se required for charge balance relative to A_2O_2Se leads to these structures having pseudo tetragonal layers based on sharing four tetrahedral edges as found for A_2O_2Te materials.

The structures of previously reported A = La–Sm materials were determined from single crystals flux-grown from the rare-earth metal, selenium and selenium dioxide.[12] Each crystallises in the non-centrosymmetric space group *Amm*2 with cell parameters of ~2*a*, *a*, *c* relative to the tetragonal A_2O_2Te structure. The structure will be discussed in more detail below, but contains infinite chains of alternating Se^{2-}/Se_2^{2-} running parallel to the *a*-axis. The *a*-axis of each material (the chain direction) is 4.7-6.5% longer than 2*b* leading to distorted A_4O tetrahedra.

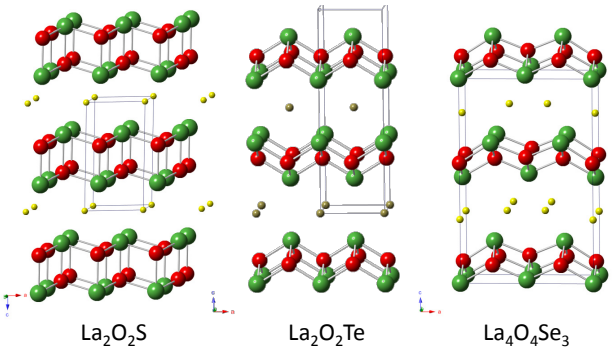

Figure 1. Structure of α-$La_4O_4Se_3$ and its relationship to La_2O_2S and La_2O_2Te. La = green, O = red, S/Te/Se = yellow.

In this work we have developed a different synthetic route to $A_4O_4Se_3$ materials which allows access to bulk samples with smaller rare earths (down to Yb) than could be prepared previously. This has revealed a complex set of closely-related structure types across the series which we label as the α, β, γ and δ-$A_4O_4Se_3$ structures. The structural properties, thermal expansion and possibilities for anion disorder are discussed for each system, and magnetic/optical properties reported for selected examples.

Experimental Section

Synthesis. $A_4O_4Se_3$ (A = Nd, Sm–Er, Yb & Y) materials were synthesised from a 2:3 molar ratio A_2O_3 and Se powders with a stoichiometric quantity of Al to act as an oxygen getter (forming Al_2O_3 in the process). ~0.5 g total mass of A_2O_3 and Se were weighed to within ±0.0001 g, ground together using an agate pestle and mortar, and placed in a 7 mm alumina crucible. Al powder was placed in a second crucible and both were sealed inside an 11 mm internal diameter silica tube under a pressure of 0.01 mbar. Sealed tubes were heated in a muffle furnace, with the following heat cycle: ramp at 5 °C min^{-1} to 600 °C and dwell for 12 hours, ramp at 0.5 °C min^{-1} to 800 °C and dwell for 1 hour, ramp at 1 °C min^{-1} to either 900 or 950 °C (synthesis temperature *T*) and dwell for the time as shown in Table 1 before furnace-cooling to room temperature.

Single Crystal Structure Analysis. Single crystals of $Eu_4O_4Se_3$ were grown by placing 0.2 g of polycrystalline $Eu_4O_4Se_3$ in an alumina crucible along with 0.1143 g of CsI to act as a flux. The crucible was sealed inside an evacuated silica ampoule, ramped at 1 °C min^{-1} to 900 °C, held for 72 hours, cooled at 0.05 °C min^{-1} to 400 °C, before furnace cooling to room temperature. The contents were washed with water to remove CsI. Plate-like crystals were formed. Single crystal X-ray diffraction data were collected at 120 K using a Bruker AXS Smart 6000 diffractometer with Mo $K\alpha_1$ radiation. Generator settings of 35 kV and 50 mA were used to reduce problems with $\lambda/2$ contamination. Temperature control was achieved using an Oxford Cryosystems cryostream. All crystals examined showed signs of twinning.

A total of 2070 frames were collected on a ~60:40 twin in ω steps of 0.3° using a data collection time of 10 s. Data were processed using GEMINI and SAINT.[19] Structure refinements were carried out using the CRYSTALS software package.[20]

Powder Diffraction. Laboratory X-ray powder diffraction data were collected using a Bruker D8 diffractometer operating in reflection mode with Cu $K\alpha_{1,2}$ radiation, a lynxeye Si strip PSD and an Oxford Cryosystems PheniX cryostat. Samples were sprinkled onto Si zero-background slides covered with a thin layer of Vaseline. Room temperature data for Rietveld refinement were collected for 12 hours over the 2θ range 5–120°; variable temperature scans to measure thermal expansion were measured for 20 minute at 5 K intervals on cooling and warming between 12 and 300 K. Powder diffraction data were analysed by the Rietveld method using the Topas Academic (TA) software[21, 22] controlled using local subroutines. High resolution synchrotron powder diffraction data were collected using beamline 11-BM at the Advanced Photon Source (APS), Argonne National Laboratory using an average wavelength of 0.413850 Å. Discrete detectors covering an angular range from -6 to 16° 2θ were scanned over a 34° 2θ range, with data points collected every 0.001° 2θ at a scan speed of 0.01°/s.[23, 24] Samples were diluted with amorphous SiO_2 to keep absorption μr to < 1.5 cm^{-1} and sealed inside polyimide capillaries.

Magnetic measurements were carried out using a Quantum Design SQUID magnetometer in the temperature range 2–300 K on samples (c.a. 0.1 g) mounted in gelatin capsules.

Diffuse reflectance spectra were obtained by illuminating a sample ground with dry NaCl (~25% w/w) using an Energetiq LDLS EQ-99 broadband lamp and collected at 20° to the excitation using an Ocean Optics Maya Pro 2000 spectrometer. Data were recorded using the Ocean Optics software and integration times were adjusted to afford maximum response of the spectrometer without saturating the detector. NaCl was used as a reference. The data were used to calculate the reflectance spectra R and the absorptance A (~1-R) and the band gap (E_g) was derived from the A - $\hbar\omega^{1/2}$ or A - $\hbar\omega^2$ curves according to the indirect/direct band gap models.[25]

Electronic structure calculations for $Eu_4O_4Se_3$ were performed within the *ab initio* density functional theory (DFT), plane-wave, pseudo-potential formalism as implemented in the CASTEP[26, 27] code. The structure model used was that obtained from refinements reported here. The electronic wave functions were expanded in a plane wave basis set up to a kinetic energy cut off of 550 eV. The electron-ion interactions were described using ultrasoft pseudo potentials from the CASTEP database. Integrations in the Brillouin zone were done with a Monkhorst-Pack k-point sampling scheme with k-points spaced at 0.04 $Å^{-1}$. The exchange-correlation functional was selected as Local Spin polarized Density Approximation (LSDA). The convergence total energy difference was set as 10^{-9} meV per atom. During the calculations a Hubbard U = 6 eV for 4*f* electrons of Eu was applied.

Results and Discussion

Phases prepared. Black polycrystalline $A_4O_4Se_3$ materials were prepared for A = Nd–Er, Yb and Y. Essentially phase-pure samples could be prepared for $R_{VIII}(A^{3+})$ down to 1.019 Å (Y^{3+}), with impurities present for the smallest A^{3+} cations as given in table 1.

Table 1. Purity of β, γ and δ-$A_4O_4Se_3$ phases (±2 %).

A^{3+}	*T* /°C	Time /h	Purity Wt %	Structure type	Main impurities
Nd	900	24	>99	α	-
Sm	900	24	>99	α	-
Eu	900	72	>99	β	-
Gd	900	12	>99	γ	-
Tb	950	12	>99	γ	-
Dy	900	12	>99	δ	-
Ho	900	12	~94	δ	Ho_2O_2Se, Ho_2O_3
Er	900	24	~72	δ	Er_2O_3
Yb	950	12	~81	δ	Yb_2O_2Se, Yb_2O_3
Y	950	12	>99	δ	-

Powder X-ray diffraction data of selected phases are shown in Figure 2. Whilst there are broad similarities between all patterns there are also a number of significant differences. Firstly, several peaks (e.g. those around 26 and 36° 2θ shaded pink in Figure 2) show clear splitting for some compositions suggesting a reduction in symmetry from orthorhombic. Secondly, some peaks which are strong for the published structure of $Nd_4O_4Se_3$ (yellow in Figure 2) are weak or absent in other phases. As discussed below, these changes reveal 4 distinct structure types for this family which we have labelled α-δ.

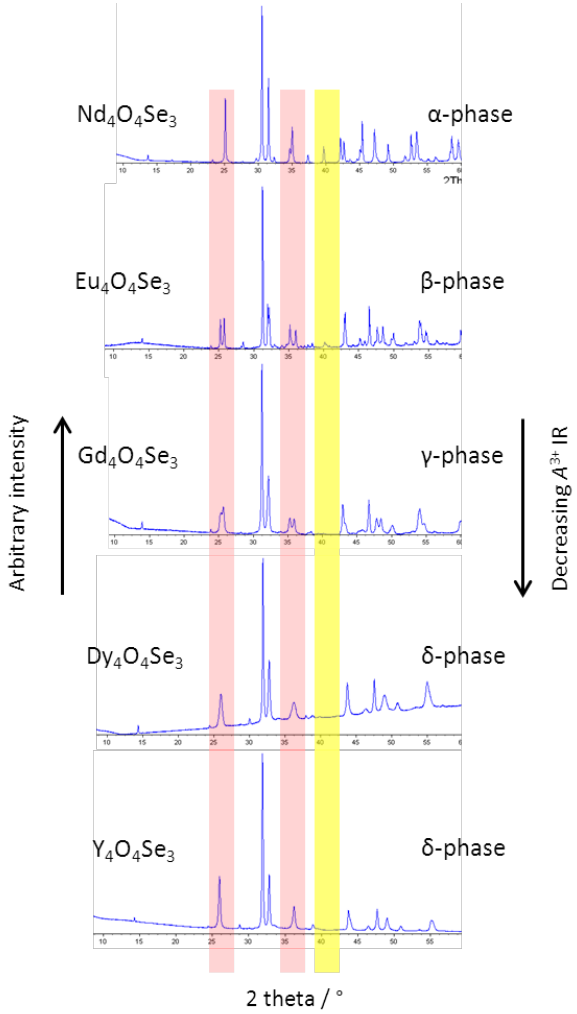

Figure 2. X-ray powder diffraction patterns for selected ionic radii $A_4O_4Se_3$ samples, obtained in Bragg-Brentano geometry using Cu $K\alpha_{1,2}$ radiation.

β-$Eu_4O_4Se_3$. Whilst the majority of peaks in the powder pattern of $Eu_4O_4Se_3$ could be indexed with a unit cell similar to known α-$A_4O_4Se_3$ materials, peak splitting of some reflections suggested a reduction in symmetry to monoclinic. The observation of several weak unindexed reflections (highlighted in Supporting Information) also indicated a doubling of the b-axis and a cell of a = 8.403986(7) Å, b = 7.808815(6) Å, c = 12.63788(1) Å with β = 91.36046(7)°. Single crystal measurements confirmed this cell and the structure was solved and refined using charge flipping and difference Fourier techniques within the Crystals software suite.[20] Crystallographic details are given in Tables 2 and 3 and derived bond distances are given in Supporting Information. The single crystal model gave an excellent Rietveld fit to synchrotron powder diffraction data, Figure 3, confirming both the structural model and phase purity of bulk samples.

Table 2. Crystallographic information for $Eu_4O_4Se_3$ from single crystal refinement.

Quantity	Value
Formula	$Eu_4O_4Se_3$
Radiation	0.71973 Å
Temperature / K	120
a / Å	8.3925(17)
b / Å	7.7949(16)
c / Å	12.618(3)
β / °	91.35(3)
Space group	$P2_1/c$
Z	4
Measured reflections	3945
Independent reflections	1681
$R_{int}(1)$	0.036
$R_{int}(2)$	0.033
h	$-10 \leq h \leq 10$
k	$-9 \leq k \leq 9$
l	$-15 \leq l \leq 15$
R	0.063
wR	0.172
gof	1.27
$\Delta\rho$ max /e Å^{-3}	5.01
$\Delta\rho$ min /e Å^{-3}	-6.06
Number of variables	46
Twin scale factors	0.585(3) 0.415(3)

Table 3. Atomic coordinates and isotropic thermal displacement parameters for $Eu_4O_4Se_3$ at 120 K.

Site	x	y	z	U_{iso}
Eu1	0.1141(3)	0.3660(6)	0.40797(15)	0.0034(5)
Eu2	0.3710(3)	0.1182(7)	0.58242(14)	0.0036(6)
Eu3	0.1141(3)	-0.1306(7)	0.40870(15)	0.0035(5)
Eu4	0.3713(3)	-0.3782(7)	0.57970(14)	0.0041(5)
Se5	0.2331(4)	-0.6233(12)	0.7402(3)	0.0057(8)
Se6	0.5252(4)	-0.6226(14)	0.7423(3)	0.0048(8)
Se7	0.1230(5)	-0.1287(11)	0.7214(3)	0.0045(8)
O8	0.372(3)	-0.101(4)	0.4833(19)	0.000(7)
O9	0.120(3)	-0.391(6)	0.4981(19)	0.005(7)
O10	0.375(3)	-0.612(6)	0.4842(18)	0.002(6)
O11	0.120(3)	0.116(7)	0.5046(19)	0.004(6)

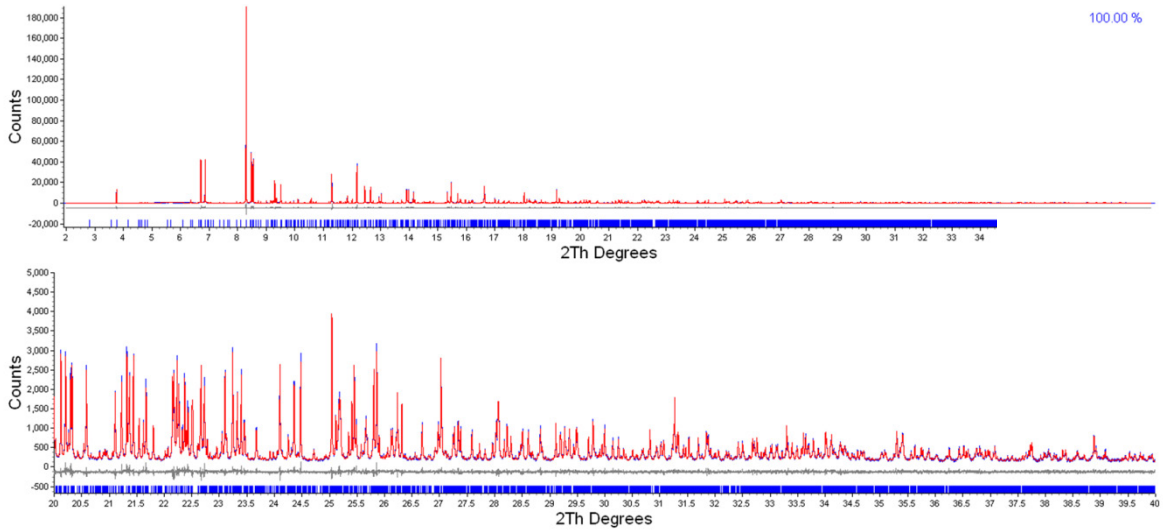

Figure 3. Rietveld refinement profile for $Eu_4O_4Se_3$, monoclinic $P2_1/c$ symmetry, a = 8.403986(7) Å, b = 7.808815(6) Å, c = 12.63788(1) Å and β = 91.36046(7)°. R_{wp} = 7.206 %, R_p = 5.197 %, R_{Bragg} = 2.365 %, gof = 1.896, recorded at 11-BM of the Advanced Photon Source with λ = 0.413850 Å. Lower plot enlarges 20–40° 2θ range.

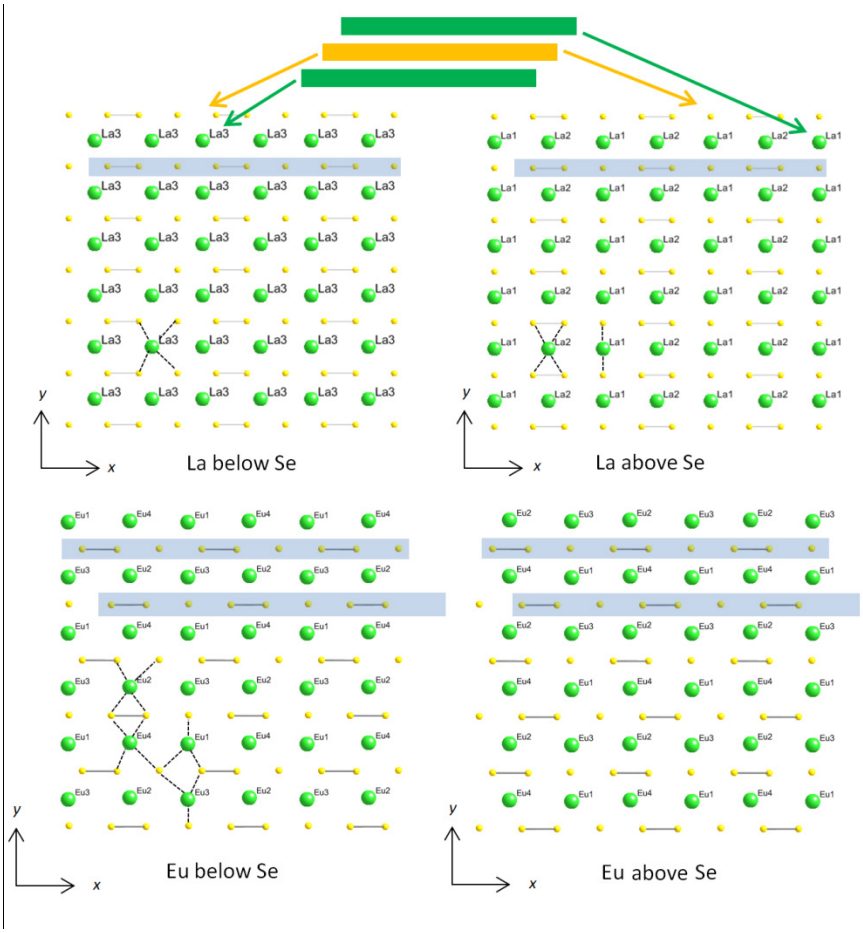

Figure 4. Single layer of Se and A viewed down [001] direction for (top) α-$La_4O_4Se_3$ and (bottom) β-$Eu_4O_4Se_3$, La/Eu = green, Se = yellow. A^{3+} sites on the left & right images are below & above the Se layers respectively. Blue highlights show Se^{2-}/Se_2^{2-} anion chains. Dashed lines show different A coordinations by Se.

The structure of β-$Eu_4O_4Se_3$ is closely related to that of α-$A_4O_4Se_3$ materials and contains layers of A_4O distorted tetrahedra sharing four edges. Eu-O-Eu bond angles for the four crystallographically unique tetrahedra range from 95.5 to 135.1°. Alternate layers are displaced by ¼ of a unit cell in the doubled [010] direction to accommodate the Se chains

leading to the observed *A*-centring. The structure contains chains of alternating Se_2^{2-} and Se^{2-} anions running parallel to the *a*-axis as found in the α-$A_4O_4Se_3$ structure. The principal structural difference between α and β is in that alternate Se chains have an offset along the a-direction in the β structure type whereas they do not in the α-structure, Figure 4.

The positions of the Se_2^{2-}/Se^{2-} chains lead to 4 distinct Eu coordination environments, which are depicted in Figure 5. Sites Eu2 and Eu4 can be described as distorted 4+4 square antiprisms with four short bonds to oxygen and 4 longer bonds to Se. Both are coordinated by an Se^{2-}, an η^1 Se_2^{2-} and an η^2 Se_2^{2-}. Eu1 and Eu3 are both 4O+3Se 7-coordinate; Eu1 is coordinated by three Se^{2-} ions and Eu3 by two Se^{2-} ions and an η^1 Se_2^{2-}. These coordination environments differ from those in α-$A_4O_4Se_3$ which contains one six ($4O + 2Se^{2-}$) and two eight ($4O + 2\eta^2\text{-}Se^{2-}$; and $4O + 2Se^{2-} + 2\eta^1\text{-}Se_2^{2-}$) coordinate A^{3+} sites. A-site coordination flexibility is clearly important in allowing these two different ordered structure types. The Se–Se bond length, 2.451(5) Å, is similar to those in the α structures which range between 2.446 (Sm) and 2.465 (Pr) Å.

γ-$A_4O_4Se_3$ (A = Gd, Tb). Gd and Tb phases retain the clear splitting of the reflections (the 102 and 10-2 reflections) around 26° 2θ seen for A = Eu, but show no reflections at ~40° 2θ and none of the weak reflections requiring a doubled b axis. As such all peaks could be indexed with a unit cell of $a \approx 4.2$ Å, $b \approx 3.9$ Å, $c \approx 12.6$ Å and $\beta = 91°$. Systematic absences were consistent with space group *A*2/*m* (*a* cell parameter is thus approximately half that of the α structure) and an excellent Rietveld fit could be achieved using the structural model given in Table 4. The final Rietveld fit for A = Gd is given in Figure 6 and that for A = Tb as Supporting Information.

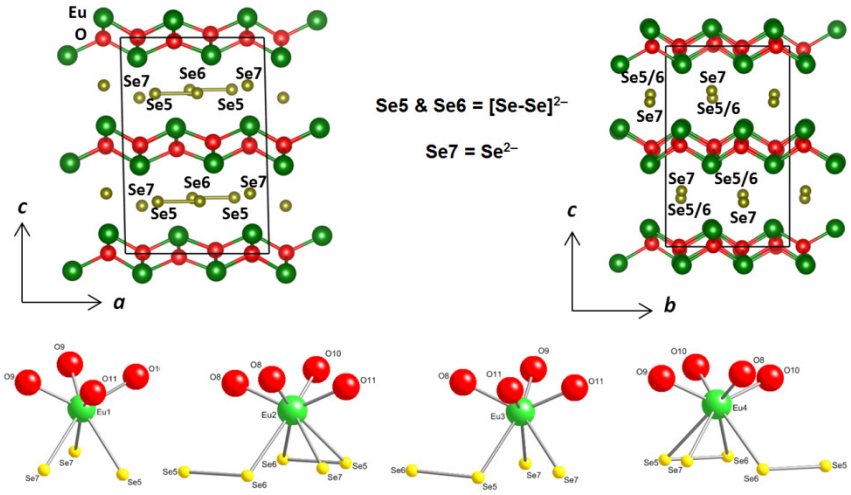

Figure 5. Structure of $Eu_4O_4Se_3$ and local Eu coordination environments. Se_2^{2-}/Se^{2-} anion chains run parallel to the *a*-axis.

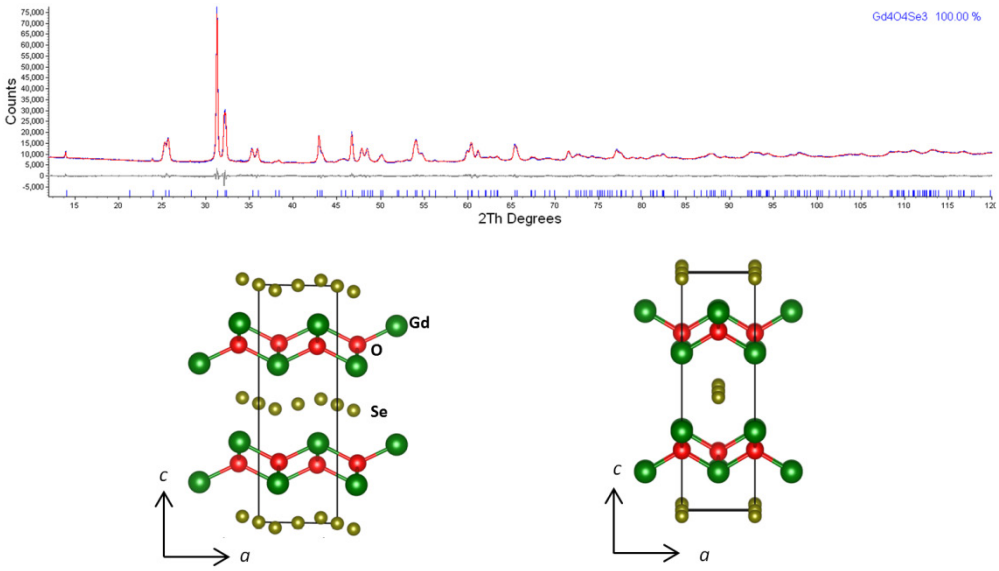

Figure 6. Rietveld fit for $Gd_4O_4Se_3$ and structural model of γ-$A_4O_4Se_3$ materials, *A*2/*m* symmetry, unit cell $a \approx 4.2$ Å, $b \approx 3.9$ Å, and $c \approx 12.6$ Å, $\beta \approx 91°$. Atoms are labeled in the figure.

Table 4. Crystallographic parameters for $Gd_4O_4Se_3$ and $Tb_4O_4Se_3$.[(a)]

	$Gd_4O_4Se_3$	$Tb_4O_4Se_3$
R_{wp}%	2.457	3.058
R_p%	1.781	2.206
R_{Bragg}%	0.958	1.110
gof	2.321	2.256
a / Å	4.1738(2)	4.1562(2)
b / Å	3.8808(1)	3.8582(1)
c / Å	12.6051(4)	12.5028(4)
β / °	90.984(4)	91.017(3)
Volume / Å^3	204.15(1)	200.46(1)
Se1 occupancy	0.475(8)	0.478(9)
Se2 occupancy	0.33(1)	0.31(1)
Se3 occupancy	0.364(7)	0.360(8)
*x*_A1	0.2439(3)	0.2450(4)
*z*_A1	0.6639(1)	0.6644(1)
*x*_Se3	0.209(2)	0.212(3)
*z*_Se3	-0.0226(3)	-0.0270(4)
*x*_O1	0.257(2)	0.251(3)
*z*_O2	0.2547(6)	0.2543(7)
B_{iso}_A1 / Å^2	0.44(2)	1.02(2)
B_{iso}_Se1 / Å^2	0.9(2)	2.8(2)
B_{iso}_Se2 / Å^2	0.01(28)	0.2(3)
B_{iso}_Se3 / Å^2	0.8(2)	2.8(2)
O1 B / Å^2	0.6(2)	2.1(2)
Refined Se composition	3.07(4)	3.15(5)

[(a)]A1, Se3 and O1 at (*x*, 0, *z*), Se1 at (0.5, 0, 0), Se2 at (0, 0, 0). Space group *A*2/*m*.

The structure of γ-$A_4O_4Se_3$ is closely related to those of the α and β phases, containing essentially identical $[A_2O_2]^{2+}$ layers but with "wave like" chains of Se between the layers running parallel to the *a*-axis. The anion chain observed cannot be interpreted in terms of a simple ordered array of Se^{2-} and Se_2^{2-} and is discussed in more detail below.

δ-$A_4O_4Se_3$ (A = Dy, Ho, Er, Yb, Y). The smallest rare earths and Y phases showed diffraction patterns very similar to those of γ-$A_4O_4Se_3$. No splitting of the 26° 2θ peak was observed for any of these samples, though broadening of this and other reflections was visible. Excellent Rietveld fits (see Supporting Information) could be achieved for all samples using a model closely related to the γ structure in the orthorhombic space group *Amma* with a ≈ 4.1 Å, b ≈ 3.8 Å, c ≈ 12.4 Å. Where required A_2O_3 and A_2O_2Se impurities were modelled as additional phases. Cell parameters and refined coordinates for each phase are given in Table 5. The anion chains of this model are very similar to those of γ-$A_4O_4Se_3$.

Table 5. Crystallographic parameters for $A_4O_4Se_3$ extracted from Rietveld analysis in space group *Amma*.[(a)]

	$Dy_4O_4Se_3$	$Ho_4O_4Se_3$	$Er_4O_4Se_3$	$Yb_4O_4Se_3$	$Y_4O_4Se_3$
R_{wp}%	1.104	2.790	2.640	2.935	8.629
R_p%	0.735	1.904	1.821	2.032	6.663
R_{Bragg}%	0.334	1.020	0.828	0.660	2.866
gof	2.630	5.910	6.282	4.628	1.488
a / Å	4.1352(2)	4.1126(1)	4.0919(1)	4.0565(1)	4.12056(6)
b / Å	3.8319(1)	3.8073(1)	3.78584(6)	3.74734(9)	3.81474(4)
c / Å	12.4455(5)	12.4021(4)	12.3468(2)	12.2102(4)	12.4212(1)
Volume / Å^3	197.11(1)	194.19(1)	191.205(7)	185.610(9)	195.247(4)
Se1 Occupancy	0.331(7)	0.378(7)	0.384(7)	0.345(8)	0.335(2)
Se2 Occupancy	0.420(8)	0.355(6)	0.372(7)	0.359(8)	0.372(2)
*z*_A1	0.8352(1)	0.8354(1)	0.83560(9)	0.8358(1)	0.83422(4)
*z*_Se1	0.5261(5)	0.5240(4)	0.5240(4)	0.5220(5)	0.5221(1)
*z*_O1	0.2509(7)	0.2486(6)	0.2423(5)	0.2418(8)	0.2433(2)
B_{iso}_A1 / Å^2	0.47(3)	1.02(3)	0.24(3)	1.14(3)	0.680(9)
B_{iso}_Se1 / Å^2	2.2(2)	3.8(2)	2.7(2)	2.3(3)	2.18(6)
B_{iso}_Se2 / Å^2	3.0(3)	1.7(2)	1.7(2)	2.3(3)	1.64(5)
B_{iso}_O1 / Å^2	1.0(2)	3.0(2)	0.07(18)	2.0(3)	0.18(5)
Refined Se composition	3.01(4)	2.93(4)	3.02(4)	2.82(5)	2.83(1)

[(a)]A1 at (0.25, 0, *z*), Se1 (0.25, 0, *z*), Se2 (0, 0, 0.5), O1 (0.25, 0, *z*).

Thermal Expansion Properties. Variable temperature powder diffraction measurements were recorded for the new phases to investigate thermal expansion properties. Data were also recorded for A = Nd as an example of the α structure type. Approximately 60 data sets recorded between 12 and 300 K were analysed for each phase by Rietveld refinement and cell parameters extracted. All samples showed a smooth variation in cell parameters over the whole temperature range (see Supporting Information) with no evidence of structural phase transitions. Volume coefficients of expansion ranged from $+1.746(9) \times 10^{-5}$ to $+2.237(3) \times 10^{-5}$ K^{-1} from 12 to 300 K. Expansion coefficients for each phase are given in Table 6.

Discussion of Structures. Each of the $A_4O_4Se_3$ structure types encountered contains essentially identical $[A_2O_2]^{2+}$ 2D layers and differ only in the arrangement of the interlayer Se^{2-} and Se_2^{2-} anions. Figure 7 shows how the Rietveld-derived cell parameters vary across the series with values normalised to the ~4.1 Å × 3.9 Å × 12 Å cell of the δ phase; cell parameters for α-$A_4O_4Se_3$ (A = La, Pr, Ce) are those reported by Strobel.[12] There is a relatively smooth decrease in cell volume with decreasing ionic radii of the A^{3+} cation across all 4 structure types. The α and δ/γ structures perhaps show a small difference in gradient of cell parameters as a function of ionic radius, which would coincide with the change in order of the selenide layers.

Table 6. Volume coefficient of thermal expansion determined from X-ray powder diffraction from 12 to 300 K.

Composition	$\alpha_V / \times 10^{-5}$ K^{-1}
$Nd_4O_4Se_3$	2.237(3)
$Sm_4O_4Se_3$	2.076(5)
$Eu_4O_4Se_3$	1.789(3)
$Gd_4O_4Se_3$	1.85(1)
$Tb_4O_4Se_3$	1.746(9)
$Dy_4O_4Se_3$	2.19(1)
$Ho_4O_4Se_3$	1.948(4)
$Er_4O_4Se_3$	2.063(4)
$Y_4O_4Se_3$	1.798(3)

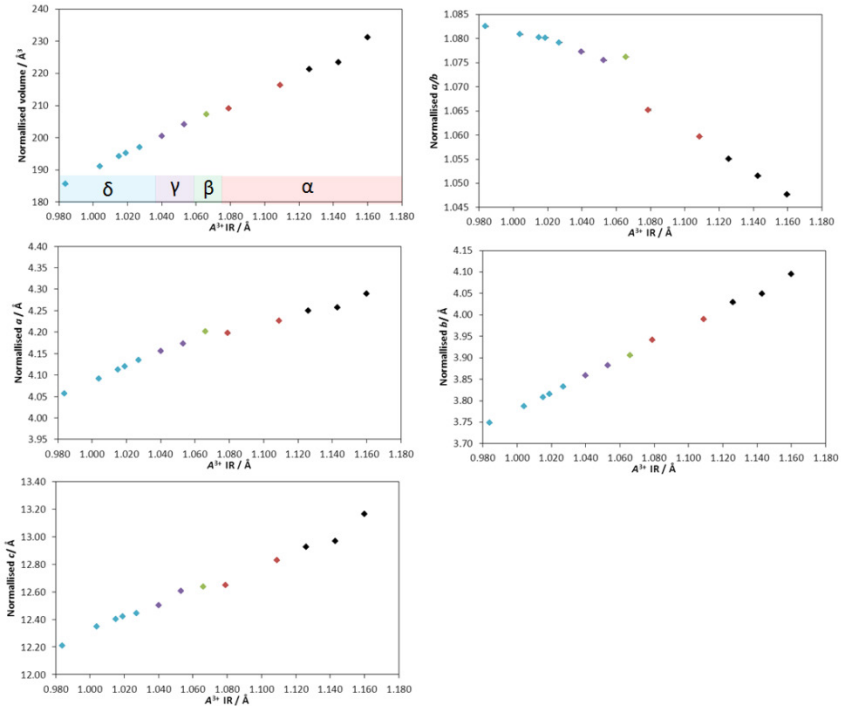

Figure 7. Normalised unit cell parameters for the α, β, γ and δ structure types as a function of the ionic radius of the A^{3+} cation.

Ordered chains of alternating Se^{2-}/Se_2^{2-} anions are observed in both the α and β structure types. The periodicity of the chain along the *a*-direction is such that it repeats every second A^{3+} ion. For example in Figure 8a each Se_2^{2-} unit is η^2 bonded to alternate A^{3+} sites in the layer below the chain. In the α structure every anion chain (i.e. above/below the plane of the figure) has the same relative shift in the a direction leading to the polar *Amm*2 structure, with exclusively " Se–Se(Se)Se–Se " configurations; that is Se_2^{2-} units lie closer to the layer below the chain and Se^{2-} closer to the layer above. In the β structure the chain at y = 0.5 is shifted by ~2 Å in the *a*-direction such that the Se_2^{2-} unit is η^2 coordinated to an A^{3+} ion in the layer above. This shift leads to a doubling of the b-axis, and the presence of both Se–Se(Se)Se–Se and Se–Se–Se(Se–Se) chains ("↑" and "↓") leads to a non-polar structure. The relative shifts of adjacent chains change the average Se coordination number of A^{3+} from $3^1/_3$ (2,4,4) in the α structure to 3.5 (3,3,4,4) in the β structure [using bonds <3.5 Å]. The energy penalty for this change in the relatively flexible coordination environment of A^{3+} appears low.

It is clear from Figure 8a that one could equally shift the selenium chain origin by ~4 Å along [100] such that the first Se_2^{2-} drawn becomes η^2-bonded to the next A^{3+} cation in the layer below, or ~6 Å so it η^2-bonds to the next-but-one A^{3+} cation in the layer above. If one superimposes these four possible chain origins one would create a pattern of Se sites as in Figure 9 with a periodic zig-zag wave of Se. This 'wave' is remarkably similar to the Se distribution determined in the disordered models of the γ and δ structures. It therefore seems likely that these materials again contain ordered individual Se^{2-}/ Se_2^{2-} chains, but that the relative offset of these chains is disordered on the X-ray length scale.

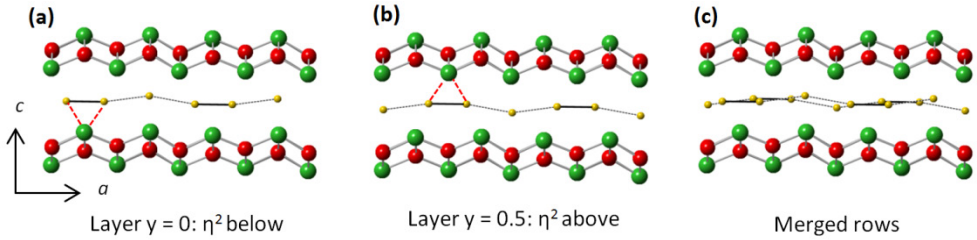

Figure 8. Ordered anion chain displacements along [100] adopted in β-$Eu_4O_4Se_3$ viewed down [010]. A = green, O = red, Se = yellow. Se_2^{2-} units identified by solid black lines, non-bonded chain interactions between Se^{2-} and Se_2^{2-} marked by dashed lines. η^2 interaction shown in red.

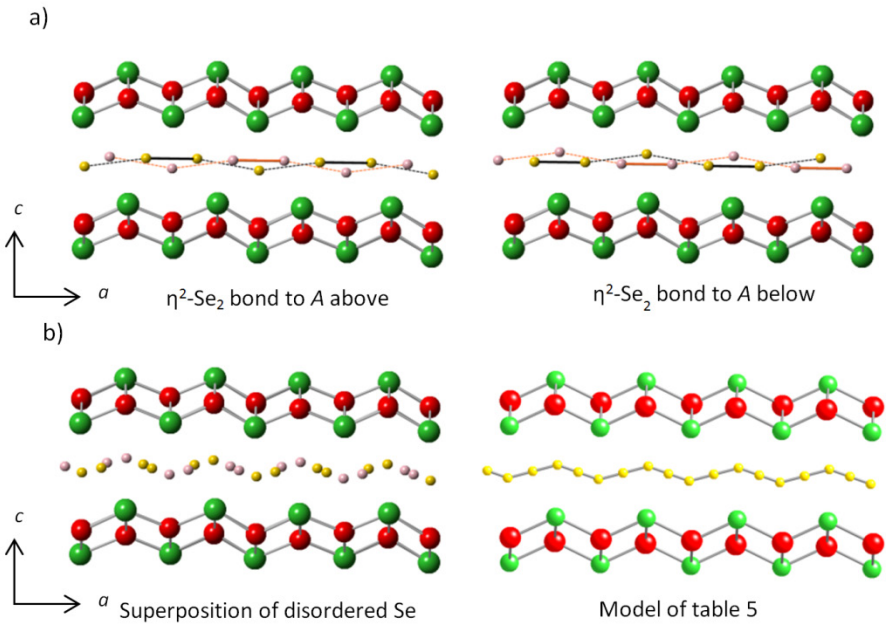

Figure 9. a) Possible ordered anion chain displacements along [100] adopted in γ & δ-$A_4O_4Se_3$ with 4 chain positions, b) comparison of superimposed anion chains with disordered anion model of γ and δ-$A_4O_4Se_3$.

Recent work on the preparation of nanoplatelets of $A_4O_4Se_3$ has suggested that they may be Se-deficient for the smaller rare earths. Rietveld refinement of Se fractional site occupancies gave Se occupancies within three standard uncertainties of 3.0 for Gd and Tb γ phases and Dy-Er δ phases. The refined Se content of Yb and Y materials were 2.82(5) and 2.83(1) giving evidence of slight Se deficiency; small amounts of Se could also be seen on the tube walls after some syntheses. The models of Figures 8 and 9 suggest one possible scheme for accommodating this deficiency. The chain in the central panel of Figure 8 alternates $Se^{2-}/Se_2^{2-}/Se^{2-}/Se_2^{2-}/Se^{2-}$. One could conceptually imagine a local disproportionation reaction $Se_2^{2-} \rightarrow Se^{2-} + Se$ with a small anion positional shift giving a local Se^{2-} coordination environment similar to that of other Se^{2-} sites. The Se produced could 'migrate' along the chain converting an adjacent Se^{2-} to Se_2^{2-} forming a defect of the type $Se^{2-}/Se^{2-}/Se_2^{2-}/Se^{2-}/Se_2^{2-}$. Each such defect would eliminate a single Se from the structure, would be of low energy, and could eliminate local strain for the smaller rare earths where the $A_4O_4Se_3$ composition is less stable.

Diffuse Reflectance Measurements. Diffuse reflectance spectra for each sample are included in Supporting Information. From a band structure view, the energy difference between the highest point of the valence band and the lowest point of conduction band is defined as the band gap E_g of the material. If the two points are at the same **k**-vector line, the band gap is direct; otherwise it is indirect. According to the different band gap types [direct band gap $E_g(d)$ or indirect band gap $E_g(i)$], the absorbance A shows different trends as a function of photon energy.[25]

$$A_d = C_d[\hbar\omega - E_g(d)]^{\frac{1}{2}}$$
$$A_i \approx C_i[\hbar\omega - E_g(i)]^2 \quad (1)$$

where C is the coefficient, and i and d indicate the direct or indirect band gap respectively. However, it is often difficult to determine the band gap type directly from diffuse reflectance measurements and a band gap higher than the true gap may be recorded. We therefore choose to derive E_g from both A - $\hbar\omega^{1/2}$ and A - $\hbar\omega^2$ curves (see the supporting information). These are listed in Table 7.

Several sharp absorptions are observed for $Dy_4O_4Se_3$ and $Er_4O_4Se_3$ samples. For $Dy_4O_4Se_3$ the absorption peaks are 1.32, 1.33, 1.34, 1.36, 1.37 and 1.38 eV. For $Er_4O_4Se_3$ the absorption peaks are 1.20, 1.22, 1.24, 1.25, 1.26 and 1.27 eV. These absorptions are due to *f-f* transition of Dy^{3+} and Er^{3+} ions.

Table 7. Band gap of $A_4O_4Se_3$ from A - $\hbar\omega^{1/2}$ and A - $\hbar\omega^2$ curves. (Unit: eV)

A	E_g(d)	E_g(i)
Eu	1.26	1.09
Gd	1.46	-
Tb	1.38	1.06
Dy*	1.32	-
Ho	1.34	1.02
Er*	1.35	1.13
Yb	1.37	1.07
Y	1.28	-

*Sharp absorptions exist.

Magnetism. Magnetic susceptibility data for the high purity samples A = Eu, Gd, Tb and Dy are shown in Figure 10 and extracted parameters in Table 8. For A = Gd–Dy the samples showed an excellent fit to the Curie-Weiss law above 50 K with high temperature effective magnetic moments, μ_{eff}, close to expected values and Weiss temperatures of –17 to –27 K

suggesting antiferromagnetic exchange interactions. Each sample shows a down turn in susceptibility at low temperature consistent with antiferromagnetic ordering below a Néel temperature, T_N, of 7–9 K. For $Eu_4O_4Se_3$ the magnetic susceptibility levels off at low temperature and we see a marked temperature dependence to the magnetic moment. This is expected for Eu^{3+} where magnetic properties are influenced by the $^7F_0$ singlet ground state and $^7F_1$ and $^7F_2$ higher states, which are separated by energies of the order of k_BT, as well as crystal field effects.[28] Similar effects are seen in, for example, Eu_2O_3.[29] The small upturn in susceptibility at very low temperatures could be caused by minor Eu(II) content. Magnetic data have previously been reported for the Ce and Nd analogues, which showed Curie-Weiss behavior at high temperature, but no long range order down to 1.8 K.[12]

Table 8. Magnetic data for $A_4O_4Se_3$ θ, μ_{eff}(300 K) extracted from fits to $\chi_m=C/(T-\theta)$ at $T > 150$ K.

A	T_N / K	θ / K	μ_{eff} (300 K) / B.M.	Term	μ_{calc} / B.M.
Eu	-		3.5	$^7F_0$	0
Gd	7	–17.2	7.91	$^8S_{7/2}$	7.94
Tb	9	–27.3	9.75	$^7F_6$	9.75
Dy	8	–22.2	10.57	$^6H_{15/2}$	10.65

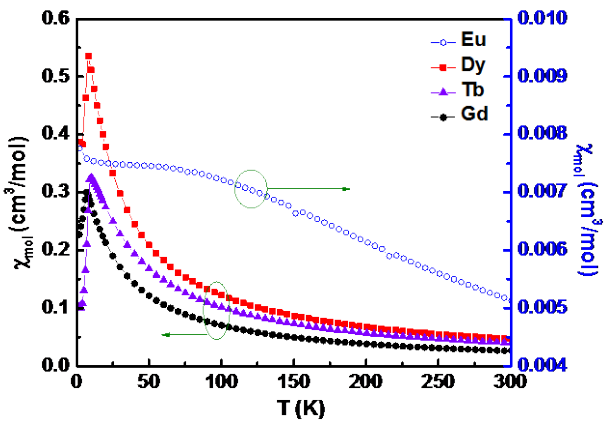

Figure 10. Molar susceptibility for $A_4O_4Se_3$ A = Eu, Gd, Tb, Dy; data for A = Eu shown on right hand axis.

Electronic band structure. The electron density differences between free atoms and the atoms in $Eu_4O_4Se_3$ were calculated to investigate bonding in $Eu_4O_4Se_3$. Two typical slices are shown in Figure SI9. The electron densities for Eu and O show significant decreases and increases, respectively. There is also a distinct boundary between Eu and O, consistent with largely ionic bonding. The increase of electron density between Se-Se and Eu-Se shows covalency for Se(I)-Se(I), Eu(III)-Se(II) and Eu(III)-[Se(I)-Se(I)] as expected. The (I) (II) and (III) indicate the ideal absolute valence state of the atoms in $Eu_4O_4Se_3$.

The spin-polarized band structure and partial density of state (PDOS) in the vicinity of the Fermi level of $Eu_4O_4Se_3$ are shown in Figure SI10 and Figure SI11. Because the LDA method often underestimates the band gap for semiconductors, the calculations predict a half-metallic[30] band structure for $Eu_4O_4Se_3$, which is a semiconductor (E_g 1.09-1.26 eV) from the diffuse reflectance result. The valence band near to the Fermi level is mainly constructed by Eu 4*f*, O 2*p* and Se 4p orbitals while the conduction band is dominated by 4*p* orbitals of Se(I)-Se(I) dimers and 5*d* orbital of Eu. Because of the different bond (valence) states for Se(I)-Se(I) and Se(II), they show considerable difference in PDOS curves.

Conclusions

Rare earth oxyselenides $A_4O_4Se_3$ (A = Nd, Sm, Eu, Gd, Tb, Dy, Ho, Er, Yb and Y) were synthesised by solid state reactions. Across the series, three new type structures (β, γ, and δ structures) were observed. $A_4O_4Se_3$ materials show the previously reported α structure type for A = Nd & Sm, the β structure for A = Eu, the γ structure for A = Gd & Tb and the δ structure for A = Dy, Ho, Er, Yb and Y. The different structures differ in the arrangement of Se^{2-}/Se_2^{2-} ions between $[A_4O_4]^{4+}$ layers. No structural phase transitions are observed for $A_4O_4Se_3$ (A = Nd, Sm, Eu, Gd, Tb, Dy, Ho, Er and Y) between 12 and 300 K and the volume coefficients of expansion ranged from $+1.746(9) \times 10^{-5}$ to $+2.237(3) \times 10^{-5}$ K^{-1} from 12 to 300 K. Diffuse reflection spectra shows $A_4O_4Se_3$ are semiconductors with band gap E_g 1.02–1.46 eV. For A = Gd, Tb and Dy, $A_4O_4Se_3$ samples show antiferromagnetic ordering with Néel temperatures, T_N, of 8 – 11 K. DFT calculations confirmed the two different valence states of Se^{2-} and Se_2^{2-} for $Eu_4O_4Se_3$.

Acknowledgements

We acknowledge the assistance of Mr Andrew Duckworth with diffuse reflectance spectra and Dr Ross Collman and Dr Johan Buurma with SQUID measurements. Use of the Advanced Photon Source at Argonne National Laboratory was supported by the U. S. Department of Energy, Office of Science, Office of Basic Energy Sciences, under Contract No. DE-AC02-06CH11357. We thank the 11-BM mail in team for their help.

Funding Sources

This work was funded by the EPSRC under EP/J011533/1.

Notes and references

[a] Department of Chemistry, University Science Site, Durham University, South Road, Durham, DH1 3LE, UK.

Corresponding Author

* John S.O. Evans. Department of Chemistry, University Science Site, Durham University, South Road, Durham, DH1 3LE, UK. Email: john.evans@durham.ac.uk.

Electronic Supplementary Information (ESI) available: [SI.docx, A4O4Se3.cif (A= Eu, Gd, Tb, Dy, Ho, Er, Yb and Y)]. See DOI: 10.1039/b000000x/

1. K. R. Reddy, K. Annapurna and S. Buddhudu, *Mater. Res. Bull.*, 1996, **31**, 1355-1359.
2. S. L. Issler and C. C. Torardi, *J. Alloy. Compd.*, 1995, **229**, 54-65.
3. C. Greskovich and S. Duclos, *Annu. Rev. Mater. Sci.*, 1997, **27**, 69-88.
4. P. N. Yocom and R. E. Shrader, *J. Electrochem. Soc.*, 1970, **117**, 91C.
5. J. Gu, Z.-Q. Zhao, Y. Ding, H.-L. Chen, Y.-W. Zhang and C.-H. Yan, *J. Am. Chem. Soc.*, 2013, **135**, 8363-8371.
6. R. D. Shannon, *Acta Crystallogr. A*, 1976, **32**, 751-767.
7. F. A. Weber and T. Schleid, *Z. Anorg. Allg. Chem.*, 2001, **627**, 1383-1388.
8. L.-B. Wu and F.-Q. Huang, *Z. Krist-new. Cryst. St*, 2007, **222**, 175-176.
9. F. A. Weber, M. C. Schurz, S. Frunder, C. F. Kuhn and T. Schleid, *Crystals*, 2012, **2**, 1136-1145.
10. O. Tougait and J. A. Ibers, *Acta Crystallographica Section C-Crystal Structure Communications*, 2000, **56**, 623-624.
11. J. Dugue, C. Adolphe and P. Khodadad, *Acta Crystallographica Section B-Structural Crystallography and Crystal Chemistry*, 1970, **B 26**, 1627-1628.
12. S. Strobel, A. Choudhury, P. K. Dorhout, C. Lipp and T. Schleid, *Inorg. Chem.*, 2008, **47**, 4936-4944.
13. H. A. Eick, *Acta Crystallographica*, 1960, **13**, 161-161.
14. Ballestr.R, *Comptes Rendus Hebdomadaires Des Seances De L Academie Des Sciences Serie B*, 1967, **264**, 1736-1738.
15. P. M. Raccah, J. M. Longo and H. A. Eick, *Inorg. Chem.*, 1967, **6**, 1471-1473.
16. F. A. Weber and T. Schleid, *Z. Anorg. Allg. Chem.*, 1999, **625**, 1833-1838.
17. E. Koyama, I. Nakai and K. Nagashima, *Acta Crystallogr. B*, 1984, **40**, 105-109.
18. P. Schmidt, O. Rademacher, H. Oppermann and S. Däbritz, *Z. Anorg. Allg. Chem.*, 2000, **626**, 1999-2003.
19. *SAINT*, (2005) Bruker AXS, Madison, WI, USA.
20. P. W. Betteridge, J. R. Carruthers, R. I. Cooper, K. Prout and D. J. Watkin, *J. Appl. Cryst.*, 2003, **36**, 1487-1487.
21. A. A. Coelho, *TOPAS Academic: General Profile and Structure Analysis Software for Powder Diffraction Data*, (2012) Bruker AXS, Karlsruhe, Germany.
22. A. A. Coelho, J. S. O. Evans, I. R. Evans, A. Kern and S. Parsons, *Powder Diffr.*, 2011, **26**, S22-S25.
23. J. Wang, B. H. Toby, P. L. Lee, L. Ribaud, S. M. Antao, C. Kurtz, M. Ramanathan, R. B. Von Dreele and M. A. Beno, *Rev. Sci. Instrum.*, 2008, **79**, 085105.
24. P. L. Lee, D. Shu, M. Ramanathan, C. Preissner, J. Wang, M. A. Beno, R. B. Von Dreele, L. Ribaud, C. Kurtz, S. M. Antao, X. Jiao and B. H. Toby, *J. Synchrotron. Radiat*, 2008, **15**, 427-432.
25. P. M. Amirtharaj and D. G. Seiler, in *HANDBOOK OF OPTICS*, eds. M. Bass, E. W. V. Stryland, D. R. Williams and W. L. Wolfe, McGRAW-HILL , INC . London, 2 edn., 1995, vol. II Devices , Measurements, and Properties.
26. M. D. Segall, P. J. D. Lindan, M. J. Probert, C. J. Pickard, P. J. Hasnip, S. J. Clark and M. C. Payne, *J. Phys. Condens. Matter*, 2002, **14**, 2717-2744.
27. S. J. Clark, M. D. Segall, C. J. Pickard, P. J. Hasnip, M. J. Probert, K. Refson and M. C. Payne, *Z. Krist.*, 2005, **220**, 567-570.
28. J. Van Vleck, *The Theory of Electric and Magnetic Susceptibilities, Clarendon*, Oxford, 1932.
29. N. L. Huang and J. H. Vanvleck, *J. Appl. Phys.*, 1969, **40**, 1144-1146.
30. R. A. Degroot, F. M. Mueller, P. G. Vanengen and K. H. J. Buschow, *Phys. Rev. Lett.*, 1983, **50**, 2024-2027.